catalysts

MDPI

*Article*

# Degradation of Organic Dye Congo Red by Heterogeneous Solar Photocatalysis with $Bi_2S_3$, $Bi_2S_3/TiO_2$, and $Bi_2S_3$/ZnO Thin Films

**Eli Palma Soto [1], Claudia A. Rodriguez Gonzalez [1], Priscy Alfredo Luque Morales [2], Hortensia Reyes Blas [1] and Amanda Carrillo Castillo [1,*]**

[1] Instituto de Ingeniería y Tecnología, Universidad Autónoma de Ciudad Juárez, Cd. Juárez CP 32310, Chihuahua, Mexico; eli.palma.uacj@gmail.com (E.P.S.); claudia.rodriguez@uacj.mx (C.A.R.G.); hortensia.reyes@uacj.mx (H.R.B.)
[2] Facultad de Ingeniería, Arquitectura y Diseño, Universidad Autónoma de Baja California, Ensenada CP 22860, Baja California, Mexico; pluque@uabc.edu.mx
* Correspondence: amanda.carrillo@uacj.mx

**Abstract:** In this work, bismuth sulfide ($Bi_2S_3$) thin films were deposited by a chemical bath deposition (CBD) technique (called soft chemistry), while titanium dioxide ($TiO_2$) nanoparticles were synthesized by sol–gel and zinc oxide (ZnO) nanoparticles were extracted from alkaline batteries. The resulting nanoparticles were then deposited on the $Bi_2S_3$ thin films by spin coating at 1000 rpm for 60 s each layer to create heterojunctions of $Bi_2S_3$/ZnO and $Bi_2S_3/TiO_2$. These materials were characterized by X-ray diffraction (XRD), scanning electron microscopy (SEM), and energy dispersive X-ray spectroscopy (EDX). The optical and contact angle analyses were undertaken by UV–Vis spectroscopy and a contact microscopy angle meter, respectively. The calculated band gap values were found to be between 1.9 eV and 2.45 eV. The $Bi_2S_3$ presented an orthorhombic structure, the $TiO_2$ nanoparticles presented an anatase structure, and the ZnO nanoparticles presented a wurtzite hexagonal crystal structure. Furthermore, heterogeneous solar photocatalysis was performed using the $Bi_2S_3$, $Bi_2S_3$/ZnO, and $Bi_2S_3/TiO_2$ thin film combinations, which resulted in the degradation of Congo red increasing from 8.89% to 30.80% after a 30 min exposure to sunlight.

**Keywords:** heterogeneous solar photocatalysis; Congo red; bismuth sulfide; semiconductor oxides; thin films



**Citation:** Palma Soto, E.; Rodriguez Gonzalez, C.A.; Luque Morales, P.A.; Reyes Blas, H.; Carrillo Castillo, A. Degradation of Organic Dye Congo Red by Heterogeneous Solar Photocatalysis with $Bi_2S_3$, $Bi_2S_3/TiO_2$, and $Bi_2S_3$/ZnO Thin Films. *Catalysts* **2024**, *14*, 589. https://doi.org/10.3390/catal14090589

Academic Editor: Anna Kubacka

Received: 30 July 2024
Revised: 24 August 2024
Accepted: 25 August 2024
Published: 2 September 2024



## 1. Introduction

Nowadays, water pollution has become a global problem due to the growth and development of modern industry [1]. Municipal and industrial wastewater is estimated to be about 2212 $km^3$ in volume. The 2017 United Nations World Water Development Report estimates that 80% of all wastewater generated by industry is discharged into the environment without prior treatment [2]. These wastewater streams contain persistent organic pollutants; organic dyes; and heavy metals, such as cobalt, copper, iron, and mercury [3].

The textile industry is one of the largest dischargers of wastewater containing organic dyes, where it releases approximately 150 billion liters of untreated wastewater into aquifers [4,5]. In these 150 billion liters of wastewater, more than 70,000 to 100,000 tons (10% to 15% of the total organic dye wastewater discharges) of various organic dyes may be dissolved [6]. These, in turn, are filtered into the aquifers, which affect the environment with a darker appearance of the water, and thus, prevent the passage of sunlight and cause a reduction in oxygen in the aquatic environment [7].

There are more than 10,000 different organic dyes in various applications [8], which are classified into natural and synthetic dyes, with the latter being divided into three categories: anionic dyes, cationic dyes, and nonionic dyes [9]. They are also classified by their chemical structures into azo dyes, anionic dyes, and indigo dyes, all of which share a

complex aromatic structure that makes them recalcitrant to the environment [10,11]. More than 60% of these dyes are aromatic azo compounds [12]. Some of these dyes are: Aniline Blue, Alcian Blue, Basic Fuchsin, Methylene Blue, Methyl Orange, Crystal Violet, Toluidine Blue, and Congo Red [13].

Congo red dye, which is an anionic diazo chromophore dye based on benzidine [14], is one of the most commonly used model dyes. It is a stable and non-biodegradable pollutant with a complex aromatic structure (see Figure 1), which makes it soluble and difficult to remove from water [15]. This dye may cause cancer, eye and skin irritation, central nervous system damage, liver damage, and drowsiness when humans are exposed to it [16].

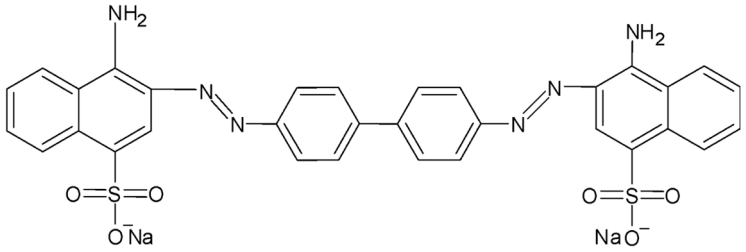


**Figure 1.** Chemical structure of Congo Red dye.

To degrade organic dyes, scientists have turned to heterogeneous photocatalysis as an emerging technology that employs the advanced oxidation process (POA). This process begins with the irradiation of a solid semiconductor material, which becomes excited, thus creating electron/hole pairs [17]. It comprises four steps for the mineralization of these organic pigments: 1—absorption of light followed by the separation of the electron/hole pair, 2—adsorption of the reagents, 3—redox reaction, and 4—desorption of the products [18]. This technology is advantageous due to its high efficiency, low operating cost, operation at ambient pressure and temperature, a requirement of no chemical additives, and environmentally friendly and non-toxic nature [19–22].

To effectively conduct heterogeneous photocatalysis on any organic pollutant, it is necessary to utilize solid semiconductors, such as metal oxides and chalcogenides as interfaces [22].

In recent years, sensitive photocatalysts, such as CuS, CdS, PbS, and $Bi_2S_3$, which are excited in the visible region with a narrow bandgap energy, have been employed to complement the more common semiconductors, like ZnO and $TiO_2$, which are activated in the ultraviolet region [23,24]. By combining these materials, various contaminants or organic dyes, such as methyl orange, rhodamine B, methylene blue, and Congo red, can be almost completely degraded [25–27].

Oxide semiconductors, such as $TiO_2$, produce an excellent photocatalyst oxidative decomposition of organic pollution under ultraviolet irradiation [27]; with a band gap energy of 3.2 eV in the anatase phase [22], this material has excellent properties, such as low cost, non-toxicity, stability chemical, and being environmentally friendly [28,29]. On the other hand, ZnO has a band gap energy of 3.3 eV [29].

Some researchers used $Bi_2S_3$ in different forms as an interface to degrade any pollutants dissolved in water. For example, Zhao [30] used $Bi_2S_3$ microspheres to degrade methyl orange (MO) at a concentration of 25 mg/L in an aqueous solution, where the experimentation consisted of irradiation with a 500 W high pressure mercury lamp using the photochemical reaction apparatus. This resulted in the degradation of MO by $Bi_2S_3$ microspheres up to 20% after 30 min.

Balachandran [31] complemented $Bi_2S_3$ with ZnO by forming a $Bi_2S_3$-ZnO nanosheet heterostructure, where this material was irradiated using four parallel medium-pressure mercury lamps that emitted a wavelength of 365 nm to degrade a concentration of 180 mg/L of AB (Acid Black); 200 mg of $Bi_2S_3$-ZnO nanosheets was placed in a reaction tube and irradiated at 365 nm to obtain 44% degradation after 30 min.

On the other hand, Bessekhouad [32] proposed complementing the $Bi_2S_3$ efficiency with $TiO_2$. For the photocatalytic degradation of an organic pollutant (Orange II), the solar box ATLAS Suntest CPS was used to simulate natural radiation, where 100 mL of 10 ppm of Orange II was mixed with 50 mg of $Bi_2S_3$-$TiO_2$, and after 30 min, the photocatalytic degradation of Orange II with $Bi_2S_3$-$TiO_2$ resulted in up to 60% removal of the pollutant. They proposed $Bi_2S_3$ as a thin film, where this nanomaterial can be used as an interface to form radicals ($\bullet OH^-$) to degrade Congo Red (CR). The advantage of this photocatalytic experiment is that the Sun was used as a source to irradiate the CR solution, where 30 min of Sun irradiation achieved up to 30.81% degradation of the CR.

For this research, metal oxide semiconductors, such as titanium dioxide ($TiO_2$) and zinc oxide (ZnO) were utilized in nanoparticles. Both are inorganic n-type semiconductors that absorb electromagnetic radiation in the ultraviolet region (UV, >400 nm) [33,34]. Additionally, metallic sulfide ($Bi_2S_3$) was employed, which is an anisotropic n-type semiconductor due to its physical properties [35]. This material is activated in the visible region (from 400 nm to 750 nm) of the electromagnetic spectrum, with a bandgap of 1.7 eV [36]. The advantage of the heterostructure is that it presents a greater efficiency when carrying out the advanced oxidation process or degradation of any contaminant [37]. Three different materials were synthesized using these materials: $Bi_2S_3$ thin films, $Bi_2S_3$ thin films coated with $TiO_2$ or ZnO nanoparticles, and $Bi_2S_3/TiO_2$ or $Bi_2S_3$/ZnO thin films.

$Bi_2S_3$ thin films were synthesized using chemical bath deposition, while $TiO_2$ was obtained using a sol–gel process assisted by a microwave and ZnO nanoparticles were extracted from alkaline batteries. These materials served as interfaces for heterogeneous solar photocatalysis, which allowed for the utilization of UV–visible regions of up to 55% of the solar radiation [38]. The resulting material's photocatalytic activity was tested by degrading Congo red dissolved in deionized water at an initial concentration of 20 ppm, which demonstrated a reduction in this model organic pollutant.

## 2. Results and Discussion

### *2.1. Characterization of $Bi_2S_3$ Thin Films Deposited with Two and Three Layers*

#### 2.1.1. Morphology of $Bi_2S_3$ Thin Films

The morphologies of the $Bi_2S_3$ thin films that consisted of two and three layers (Figure 2) resembled spherical shapes of entangled sea urchins, which were referred to as such by some authors [39], while others described them as flower-shaped microspheres [30]. In Figure 2B, crystal growth was observed compared with Figure 2A due to the third layer of the chemical bath. The methodology followed by Carrillo and collaborators [39] was entirely reproducible and resulted in the same morphology.

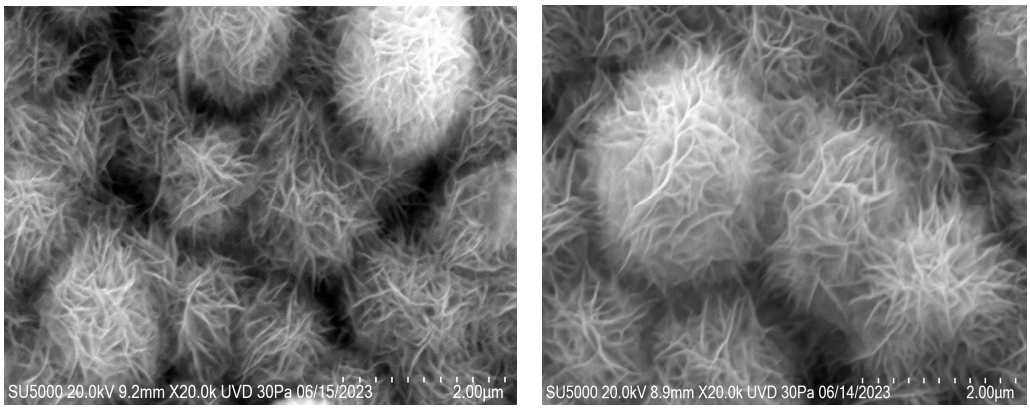


(**A**) (**B**)

**Figure 2.** SEM micrographs for $Bi_2S_3$ thin films with (**A**) two layers and (**B**) three layers deposited.

2.1.2. X-ray Diffraction of $Bi_2S_3$ Thin Films

Figure 3 displays various diffraction patterns, where the characteristic peak of the $Bi_2S_3$ thin films appears on the crystallographic plane (2 2 1), which corresponds to the orthorhombic structure. This structure aligns with the reference codes 00-017-0320 and 01-089-8965 of the X'Pert HighScore Plus calculation program, which is consistent with previously reported results [36,39–41]. Figure 3 shows that the three-layer $Bi_2S_3$ thin-film peaks were more intense due to the increased number of chemical bath depositions, which led to an increase in the crystal size from 19.4 nm to 22 nm.

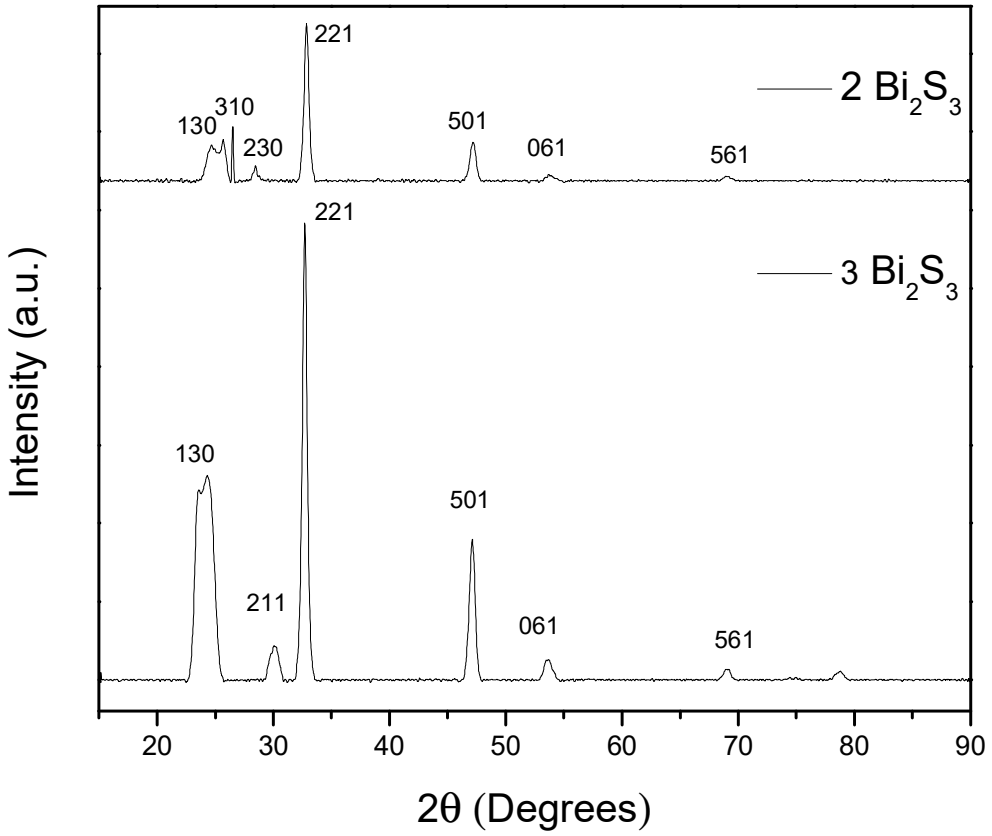


**Figure 3.** Diffractogram for $Bi_2S_3$ thin films deposited with two layers (2 $Bi_2S_3$) and three layers (3 $Bi_2S_3$).

2.1.3. Optical Characterization

The absorption spectra in Figure 4 show a shift to the right (red shift) as the number of layers increased from two to three. Also, in the range of 750 nm to 550 nm, the absorption in the two different layers showed a higher value, which indicates the possibility of excitation in the visible range. Carrillo and co-workers replicated the synthesis of such thin films, and thus, the results are similar [39,40]. The transmittance spectra can be seen in FS1.

Regarding the band gap energy, Tauc's method (see Figure 4) [42] was used and reported values of 1.9 eV and 1.95 eV were obtained, shown with blue arrows. Other authors that reproduced the same material also obtained a change in the band gap energy when increasing the number of chemical baths [43].

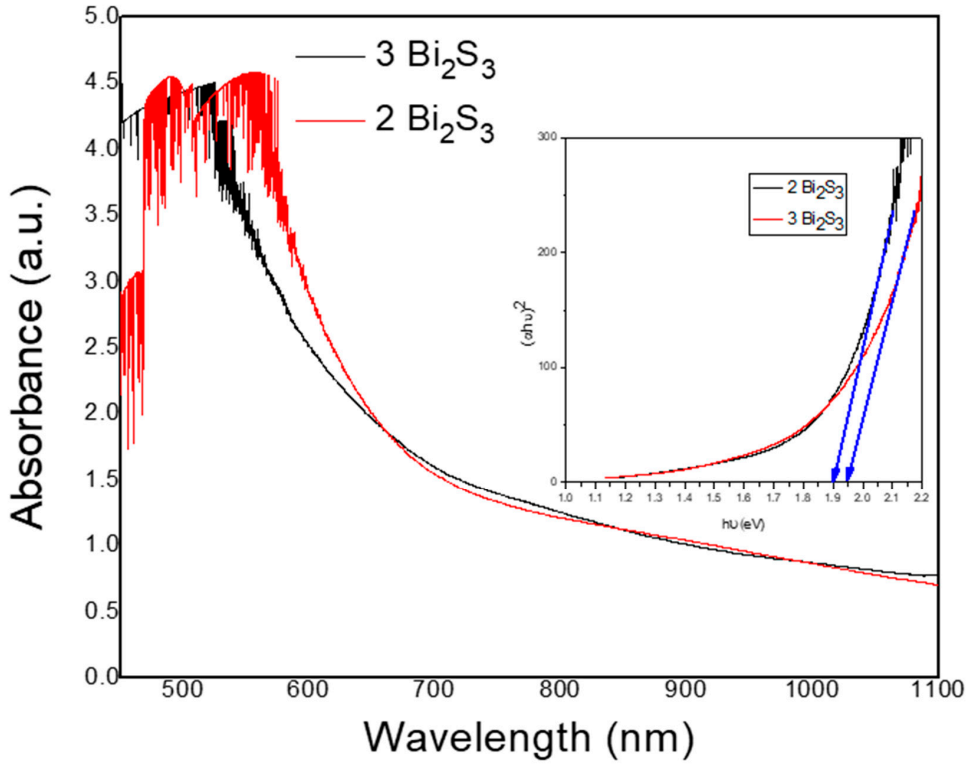


**Figure 4.** Absorption of $Bi_2S_3$ thin films and Tauc variable versus energy plot for two layers (2 $Bi_2S_3$) and three layers (3 $Bi_2S_3$).

### 2.1.4. Contact Angle of $Bi_2S_3$ Thin Films

The study of the surface wettability of the thin films indicated contact angles that ranged between 123° and 117° for the two-layer $Bi_2S_3$ thin film (Figure 5A) and three-layer $Bi_2S_3$ thin film (Figure 5B), respectively. While classified as hydrophobic films since they had contact angles with water greater than 90° [43], as the number of chemical baths increased, the angle decreased.

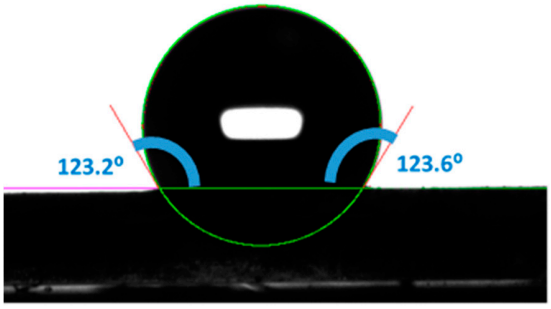


(**A**)

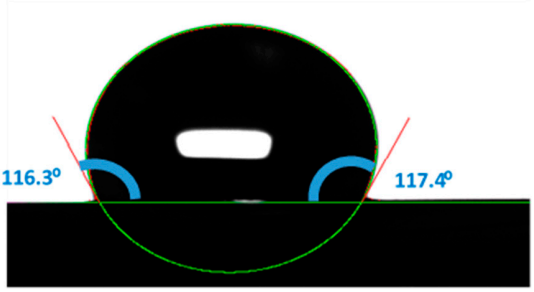


(**B**)

**Figure 5.** Contact angle of $Bi_2S_3$ thin films: deposited at (**A**) two layers and (**B**) three layers.

Thin films with contact angles classified as hydrophobic allow for higher flow and prevent saturation, which facilitates an increased formation of oxidizing radicals on the catalyst surface [44].

### *2.2. Characterization of $Bi_2S_3/TiO_2$ Thin Films*

#### 2.2.1. Morphology of $Bi_2S_3/TiO_2$ Thin Films

Figure 6 shows the micrographs of $Bi_2S_3$ thin films with $TiO_2$ nanoparticles deposition. To obtain additional insight into the topographies of the $TiO_2$ nanoparticles, the EDX analysis of the sample was performed from the same area, as shown in Figure 6A,B. The EDX analysis (Figure 6C,D) confirmed the presence of titanium oxide nanoparticles on $Bi_2S_3$ thin films. The elemental analysis of the two-layered $Bi_2S_3/TiO_2$ thin films gave ~30.28% of bismuth, ~12.01% of sulfur, ~0.22% of titanium, and ~57.49% of oxygen, and for the three-layered $Bi_2S_3/TiO_2$ thin films, the analysis gave ~30.56% of bismuth, ~11.73% of sulfur, ~0.74% of titanium, and ~56.96% of oxygen, which proved that the deposited $TiO_2$ nanoparticles were in the $Bi_2S_3$ thin films. Also, it was observed by means of EDAX analysis, as shown in Figures S2 and S3, that the elemental distributions of Bi, S, Ti, and O were homogeneous.

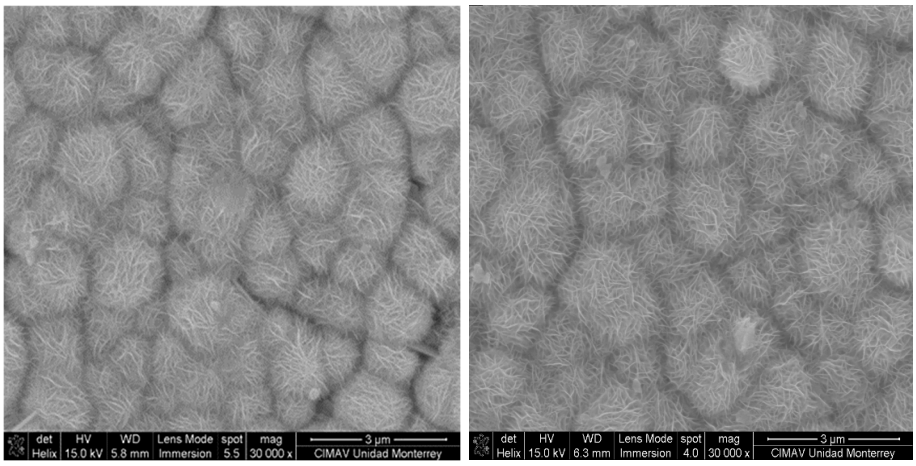


(**A**) (**B**)

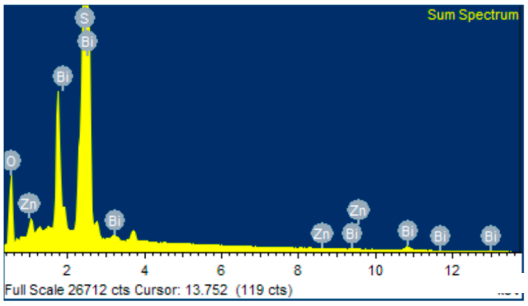


(**C**)

**Figure 6.** *Cont.*

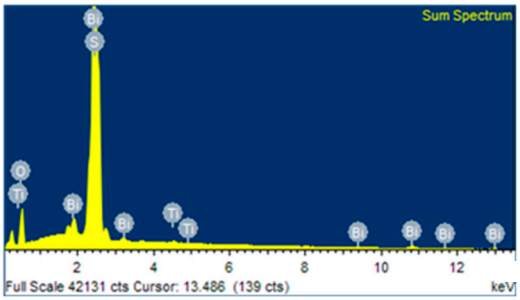


(**D**)

**Figure 6.** SEM micrographs and EDX analysis for thin films: (**A**,**C**) two-layered $Bi_2S_3/TiO_2$ and (**B**,**D**) three-layered $Bi_2S_3/TiO_2$.

### 2.2.2. X-ray Diffraction of $Bi_2S_3/TiO_2$ Thin Films

Figure 7 shows distinct intensity peaks in the diffractograms that indicate characteristic orientations of the $TiO_2$ nanoparticles. The (1 0 1) orientation corresponded to the anatase phase according to the $TiO_2$ Nps reported in [45–47] while the (2 0 2) orientation belonged to the rutile phase [46], which was located at 56.82°. These crystallographic planes are typical of $TiO_2$. The characteristic peak of $Bi_2S_3$ remained unaffected by the presence of $TiO_2$ nanoparticles, with its peak located in the (2 2 1) crystallographic plane, which corresponded to the orthorhombic structure [37].

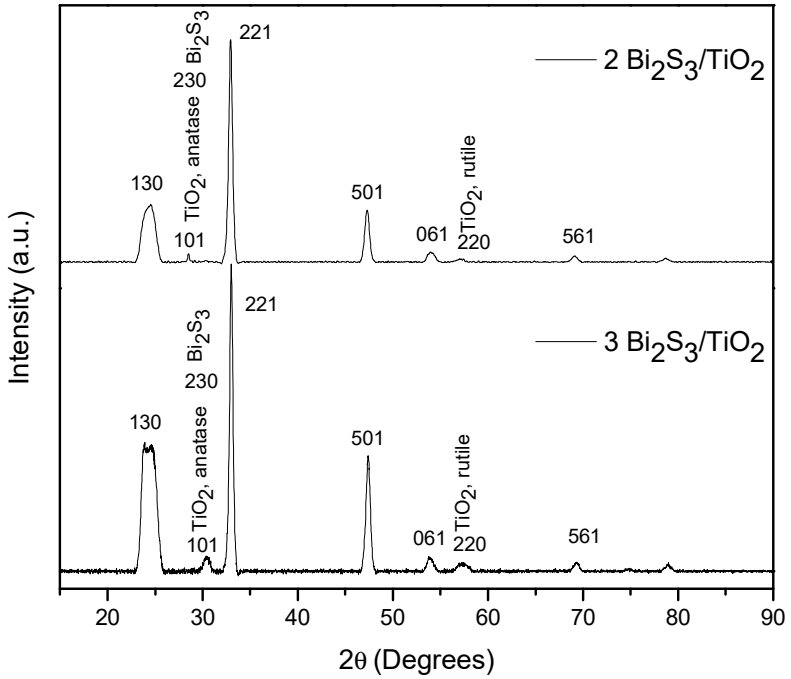


**Figure 7.** Diffractogram for thin films: two-layer $Bi_2S_3/TiO_2$ (2 $Bi_2S_3/TiO_2$) and three-layer $Bi_2S_3/TiO_2$ (3 $Bi_2S_3/TiO_2$).

The peak at 28.51° was shared by both $Bi_2S_3$ and $TiO_2$, but in different crystallographic planes. For $TiO_2$, this peak represented a (1 0 1) crystallographic orientation, while for $Bi_2S_3$, it corresponded to the (2 3 0) crystallographic plane. In the three-layered thin-film $Bi_2S_3/TiO_2$, the peaks were more closely aligned, where the orientation remained at (1 0 1) for $TiO_2$ [47] and a crystallographic (2 1 1) plane for $Bi_2S_3$.

It is worth noting that the structural composition of neither material was compromised. In the case of $Bi_2S_3$, the (2 2 1) crystallographic plane appeared more intense due to the increased number of chemical bath depositions, which attested to the purity of $Bi_2S_3$ [39].

For $TiO_2$, the anatase and rutile phases were visible through their respective characteristic peaks and crystallographic orientations, which confirmed the successful formation of a heterojunction [48].

### 2.2.3. Optical Characterization of $Bi_2S_3/TiO_2$ Thin Films

The absorption spectrum of the two-layer $Bi_2S_3/TiO_2$ exhibited a blue shift relative to the three-layer $Bi_2S_3/TiO_2$ thin film, which enabled excitation with longer wavelengths in the visible region, which was associated with electron/hole pair generation [49] The transmittance spectra can be seen in FS4.

The $TiO_2$ induced a shift toward the UV region, as shown by an absorption edge at 400 nm [28].

Both heterostructures can initiate the redox process of pollutants due to strong absorption in the visible region [48].

Figure 8 shows the bandgaps obtained using Tauc's method for the two-layer and three-layer $Bi_2S_3/TiO_2$ films, which resulted in 2.3 eV and 2.35 eV respectively, shown with blue arrows. These results indicate well-defined absorption edges and lower bandgaps compared with the findings of Serentuya and colleagues [49]. Notably, the absorption edge extended up to 650 nm, which indicates visibility in the visible region for both materials.

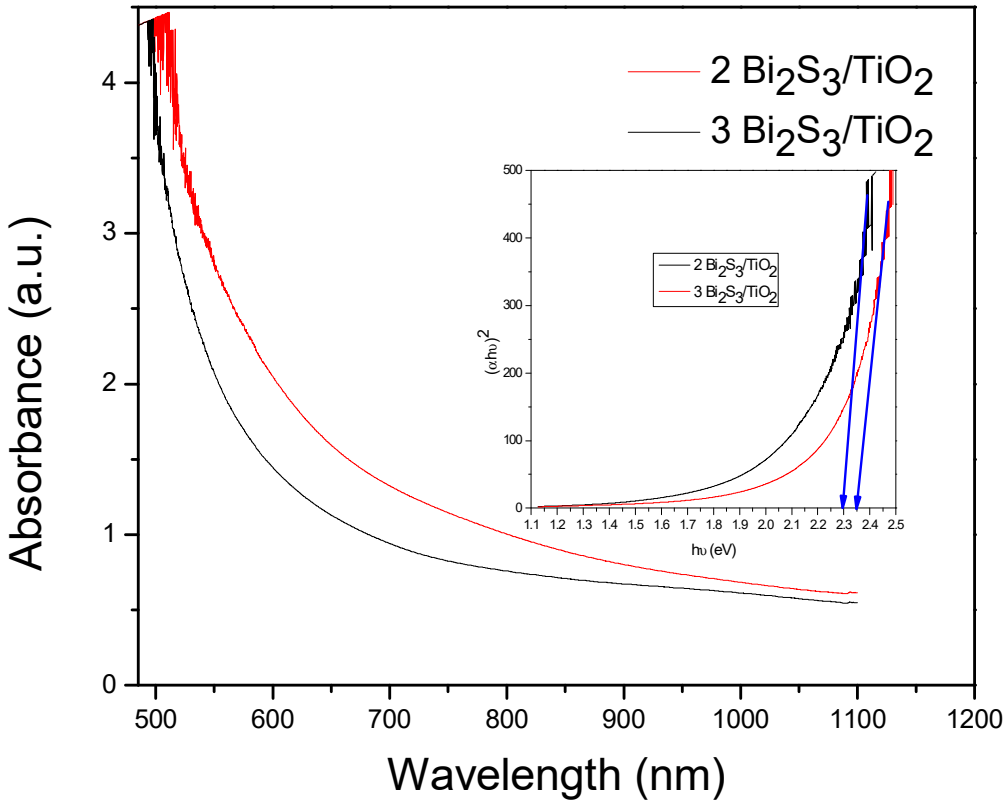


**Figure 8.** Absorption for $Bi_2S_3/TiO_2$ thin films, Tauc variable versus energy plot for two-layer $Bi_2S_3/TiO_2$ (2 $Bi_2S_3/TiO_2$) and Tauc variable versus energy plot for three-layer $Bi_2S_3/TiO_2$ (3 $Bi_2S_3/TiO_2$).

### 2.2.4. Contact Angle of $Bi_2S_3/TiO_2$ Thin Films

The contact angles of the two-layer and three-layer thin films (Figure 9A,B) showed contact angles of 95.3° to 86.0°. This means that the $TiO_2$ nanoparticles influenced the affinity to water, which shifted the three-layer $Bi_2S_3/TiO_2$ film from hydrophobic to hydrophilic. This reduction resulted in fewer hydroxyl groups being formed due to the wettability of the film surface [50].

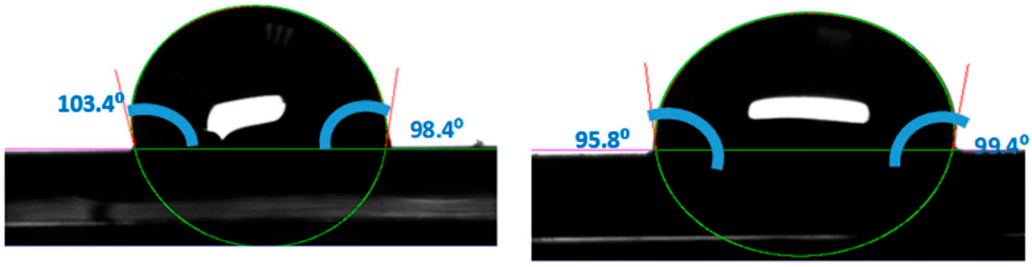


(**A**) (**B**)

**Figure 9.** Contact angle of (**A**) 2-layer $Bi_2S_3/TiO_2$ thin film and (**B**) 3-layer $Bi_2S_3/TiO_2$ thin film.

In general, the synthesized films had poor wettability, which was derived from the chemical compositions and morphologies of the materials, and thus, a similar formation of oxidizing groups was expected and a very similar degradation on the same pollutant was derived [51].

### *2.3. Characterization of $Bi_2S_3$/ZnO Thin Films*

#### 2.3.1. Morphology of $Bi_2S_3$/ZnO Thin Films

Micrographs captured at 30k magnification (Figure 10) depicted the morphology of the $Bi_2S_3$ thin films, where the nanospheres remained unaltered upon deposition of the ZnO nanoparticles. The EDX spectra of the $Bi_2S_3$/ZnO samples are shown in Figure 10C,D. The names and percentages of the elements for two layers of $Bi_2S_3$/ZnO and three layers of $Bi_2S_3$/ZnO are shown in the labeling. Additionality was observed by means of EDAX analysis, as shown in Figures S5 and S6, that the elemental distributions of Bi, S, Zn, and O were homogeneous.

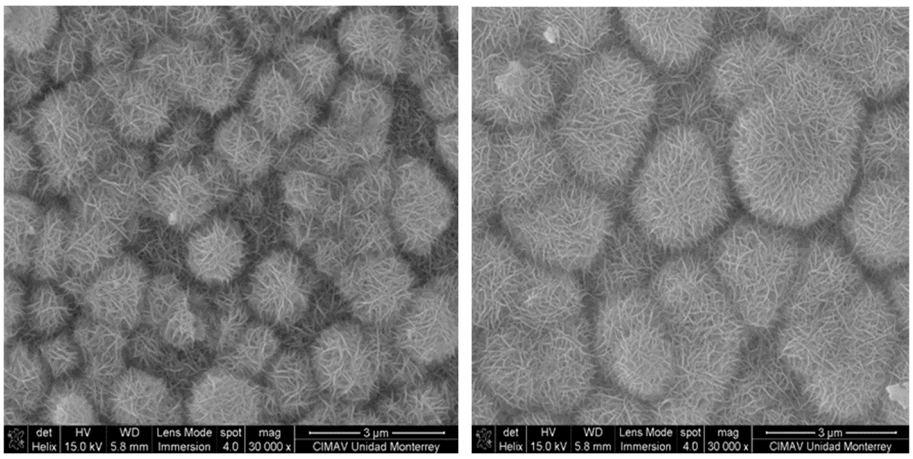


(**A**) (**B**)

| Element | Weight% | Atomic% |
|---|---|---|
| O K | 14.74 | 62.93 |
| S K | 4.21 | 8.96 |
| Zn L | 2.27 | 2.37 |
| Bi M | 78.78 | 25.74 |
| Total | 100. | |

(**C**)

**Figure 10.** *Cont.*

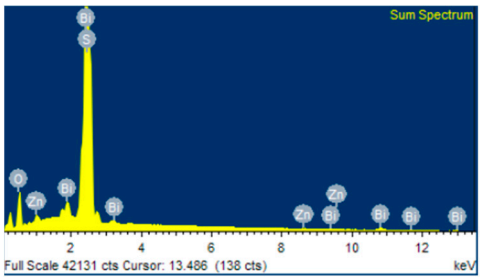


| Element | Weight% | Atomic% |
|---|---|---|
| O K | 11.33 | 55.29 |
| S K | 5.05 | 12.30 |
| Zn L | 1.41 | 1.69 |
| Bi M | 82.21 | 30.72 |
| Total | 100 | |

(**D**)

**Figure 10.** SEM micrographs and EDX analysis for thin films: (**A**,**C**) two-layer $Bi_2S_3$/ZnO and (**B**,**D**) three-layer $Bi_2S_3$/ZnO.

### 2.3.2. X-ray Diffraction of $Bi_2S_3$/ZnO Thin Films

Figure 11 displays the diffractogram peaks of the material separately, as it was considered a heterojunction, where the ZnO was deposited by spin coating and neither material was structurally modified.

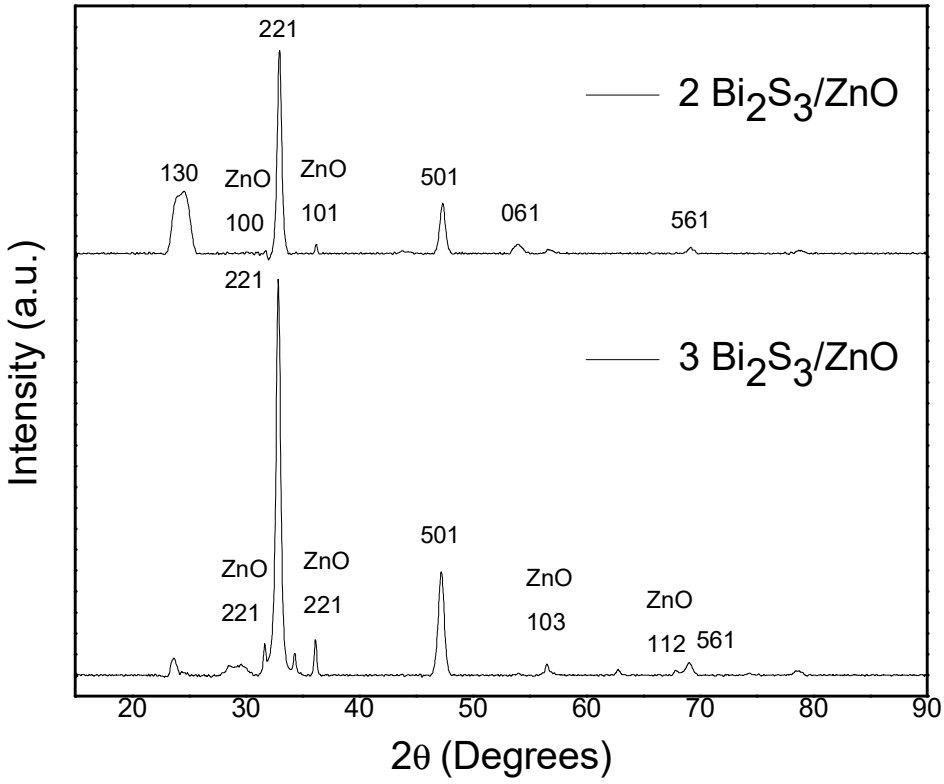


**Figure 11.** Diffractogram for two-layer $Bi_2S_3$/ZnO (2 $Bi_2S_3$/ZnO) thin films and three-layer $Bi_2S_3$/ZnO (3 $Bi_2S_3$/ZnO) thin films.

Characteristic peaks in the crystallographic planes (1 0 1) and (1 0 0) are shown for ZnO, which correspond to the hexagonal wurtzite crystal structure [52,53] according to the ZnO Nps reported in [54].

The hexagonal crystalline structure of ZnO is advantageous for photocatalysis due to its chemical stability and high refractive index [55], which leads to increased hydroxyl ion production and photoactivity [51].

### 2.3.3. Optical Characterization of $Bi_2S_3$/ZnO Thin Films

The absorption edges of the two- and three-layer $Bi_2S_3$/ZnO thin films ranged from 750 nm to 450 nm (see Figure 12). A blue shift, which indicates a shift toward shorter

wavelengths, was observed compared with the $Bi_2S_3$ thin films without ZnO. Additionally, the three-layer $Bi_2S_3$/ZnO films showed a red shift toward the visible region [56]. The addition of ZnO resulted in enhanced absorption in the visible region because it absorbed a small part of visible light near 400 nm, but it was not enough because this is the boundary of the UV and visible regions; therefore, material that absorbs light toward the visible region is required to take advantage of the source of solar radiation [53], which is one reason for expanding the photocatalytic activity of $Bi_2S_3$ thin films. The transmittance spectra can be seen in FS7.

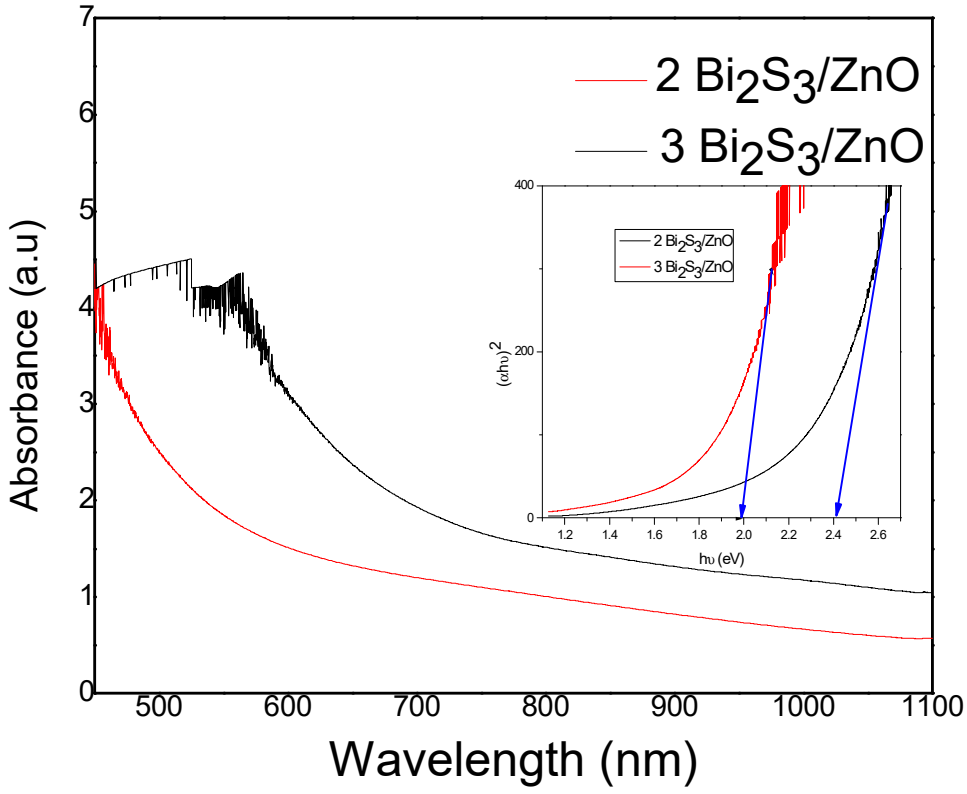


**Figure 12.** Absorption for $Bi_2S_3$/ZnO thin films and Tauc variable versus energy plots for two-layer $Bi_2S_3$/ZnO (2 $Bi_2S_3$/ZnO) and three-layer $Bi_2S_3$/ZnO (3 $Bi_2S_3$/ZnO).

The addition of ZnO enhanced the photocatalytic activity of the $Bi_2S_3$ thin films in the ultraviolet–visible spectrum such that the range of OH radical formation was broader. Hence, sunlight became a viable radiation source since it falls within the range of 450 to 700 nm [57]. Thus, photons with energies greater than those depicted in Figure 12 (2.45 eV and 2.0 eV, shown with blue arrows.) can induce radical formation, which leads to pollutant reduction. The bandgap increased significantly when ZnO was added to the $Bi_2S_3$ thin films, as the metal oxide exhibited a bandgap of 3.3 eV [54]. Al-Zahrani showed different band gaps of $Bi_2S_3$/ZnO, where the cationic concentration (the amount of positive charges present on the surfaces of materials) caused the band gap energy blue shift; in this case, this was caused by a heterostructure with anionic concentration because the materials were type n, and therefore, shifted toward the red [54].

### 2.3.4. Contact Angle of $Bi_2S_3$/ZnO Thin Films

The introduction of ZnO nanoparticles decreased the contact angle (Figure 13A,B) compared with the $Bi_2S_3$ thin films alone, which indicates a hydrophobic nature. This reduced wettability facilitates the flow of OH radicals. The contact angle values observed in this study were higher than those reported by Yu and colleagues [55], which is beneficial for ensuring effective OH radical flow.

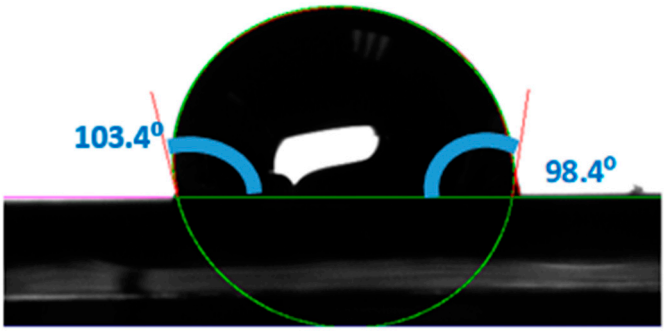


(**A**)

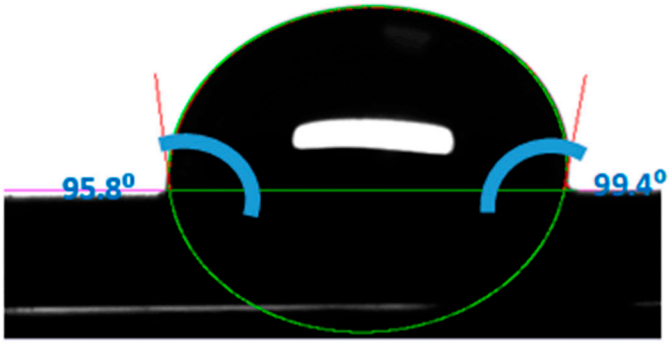


(**B**)

**Figure 13.** Contact angle for thin films: (**A**) two-layer $Bi_2S_3$/ZnO thin film and (**B**) three-layer $Bi_2S_3$/ZnO.

### *2.4. Photocatalytic Activity of $Bi_2S_3$, $Bi_2S_3/TiO_2$, and $Bi_2S_3$/ZnO Thin Films*

The photocatalytic activity of the thin films was evaluated with the degradation of the contaminant Congo red dissolved in deionized water at initial concentrations of 20,011 ppm, 20,495 ppm, and 20,373 ppm in the first, second, and third replicas, respectively. Table 1 shows the summary of each of the replicas of the photocatalytic activity exposed for 30 min with each of the different materials.

**Table 1.** Congo red degradation replicas through heterogeneous solar photocatalysis using thin films.

| Congo Red | | | | | | |
|---|---|---|---|---|---|---|
| | 1st Replica | | 2nd Replica | | 3rd Replica | |
| **Material** | **Concentration** | **% Degradation** | **Concentration** | **% Degradation** | **Concentration** | **% Degradation** |
| C initial | 20.011 | 0 | 20.495 | 0 | 20.373 | 0 |
| Two-layer $Bi_2S_3$ | 15.727 | 21.408 | 16.696 | 18.53622835 | 17.510 | 14.05291317 |
| Three-layer $Bi_2S_3$ | 15.904 | 20.523 | 16.58 | 19.10222005 | 18.560 | 8.899033034 |
| Two-layer $Bi_2S_3$/ZnO | 13.846 | 30.808 | 15.225 | 25.71358868 | 17.475 | 14.22470917 |
| Three-layer $Bi_2S_3$/ZnO | 15.237 | 23.856 | 15.264 | 25.52329837 | 17.312 | 15.02478771 |
| Two-layer $Bi_2S_3/TiO_2$ | 15.46 | 22.742 | 16.654 | 18.74115638 | 17.237 | 15.392922 |
| Three-layer $Bi_2S_3/TiO_2$ | 15.691 | 21.588 | 15.728 | 23.25933154 | 17.378 | 14.70082953 |

Figure 14 represents a graph of the three replicas showing the two $Bi_2S_3$/ZnO films with higher efficiency in the degradation of the dye; it also showed a higher standard

deviation, which indicates the variability of the degradation attributed to the incidence of solar radiation. The average for the three replicas showed a degradation from 20.33 ppm to 15.87 ppm for an efficiency of 21.93%.

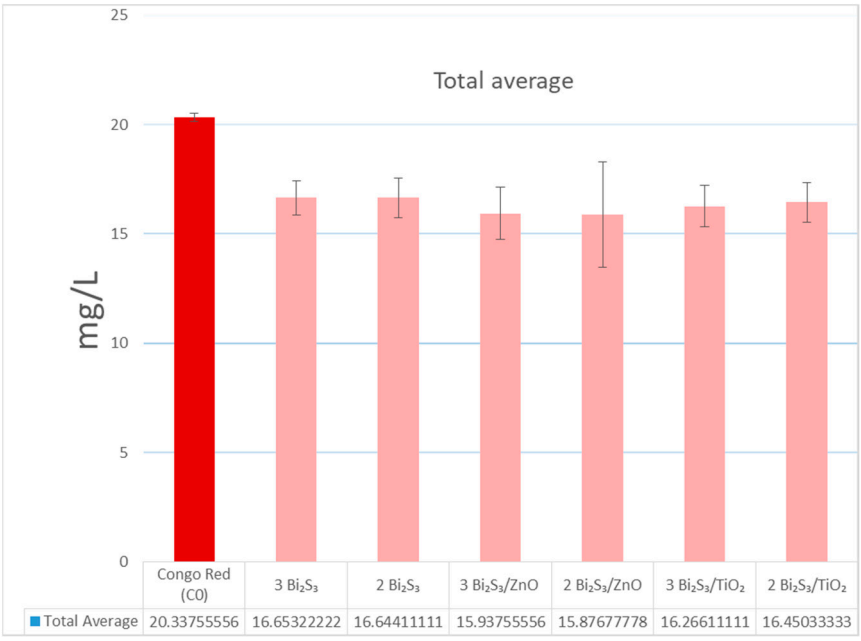


**Figure 14.** The graph indicates the standard deviations and concentrations of the three experimental replicas.

The first replica was performed on 17 May 2023 and had the highest radiation and efficiency due to the incident solar radiation of the three replicas. The material that obtained the highest degradation in the first replicas was the two-layer $Bi_2S_3$/ZnO thin film with 30.808% (applying Equation (1)) in 30 min. Figure 14 shows the decrease in absorbance and degradation kinetics.

Figure 15 shows the absorbance related to the organic contaminant degradation, which reveals a primary absorption edge at 497 nm. As the organic molecule transformed and its concentration decreased, this edge diminished. Notably, the absorbance edges showed a decreasing trend, which was characterized by a $\pi \rightarrow \pi^*$ electronic transition with a bathochromic shift (red shift), which indicates absorption at longer wavelengths [58]. The material exhibited no signs of wear or chemical reactions on the film, which was attributable to its hydrophobic nature. This stability suggests its efficacy in combating organic contaminants with complex molecular structures under natural climatic conditions.

Figure 15 shows the degradation time with the highest efficiency that was calculated and the degradation kinetics of the organic pollutant. The two-layer $Bi_2S_3$/ZnO material degraded 100% at 300 min. Equation (1) was used to describe the degradation kinetics:

$$C(t) = C_0 e^{kt} \quad (1)$$

Once Equation (1) was obtained, the values obtained from the measurements were substituted to obtain the constant k using Equation (2):

$$k = -\frac{\ln\left(\frac{C_t}{C_0}\right)}{t} \quad (2)$$

The two-layer $Bi_2S_3$/ZnO thin films obtained the highest efficiency of 30.808% (as shown in Table 2) in 30 min of solar irradiation, which indicates that the highest amount of radicals were generated to degrade the pollutant.

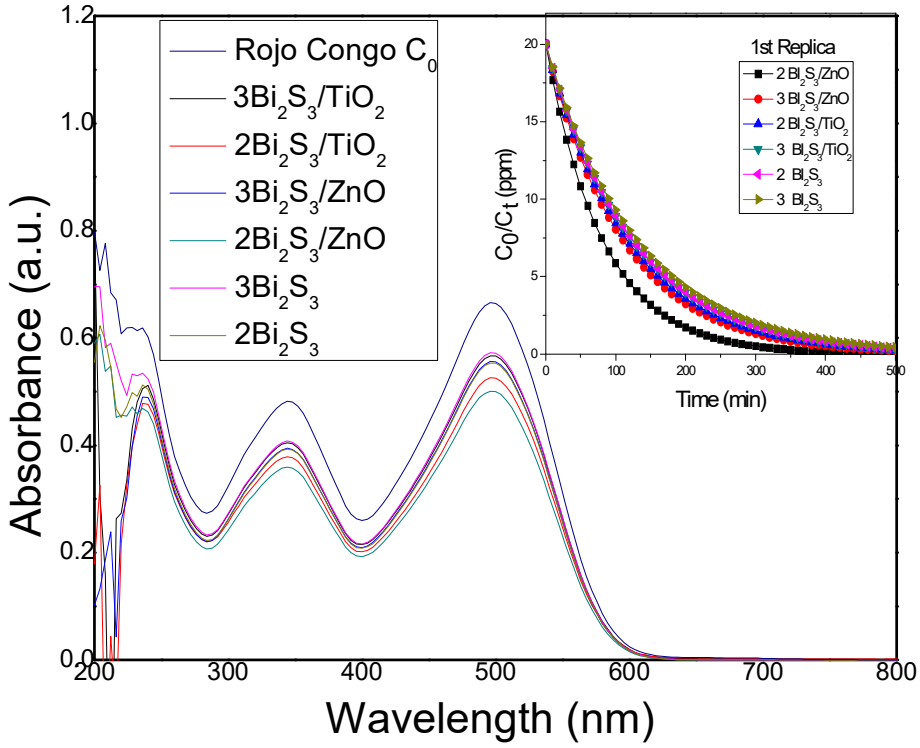


**Figure 15.** First replica absorption spectra of a solution of Congo red concentration before and after 30 min of heterogeneous photocatalysis and reaction kinetics of Congo red degradation. Second and third replicas are shown in the Supplementary Material Figures S8 and S9.

**Table 2.** Conditions of photocatalytic reaction (Ciudad Juarez Chihuahua, Mexico).

| **Conditions/Number of Replicas** | **1** | **2** | **3** |
|---|---|---|---|
| Date and time | 17 May 2023 (11:30 a.m. to 12:00 p.m.) | 19 July 2023 (12:20 p.m. to 12:50 p.m.) | 9 August 2023 (11:50 a.m. to 12:20 p.m.) |
| Solar radiation ($W/m^2$) | 1000 | 910 | 870 |
| Solar UV index | 7.12 | 11 | 10 |
| Temperature (°C) | 25 | 39 | 33 |
| Humidity (%) | 24 | 13 | 26 |
| Initial concentration (Co) (mg/L) | 20.011 | 20.495 | 20.373 |

The absorption edges provide insight into a potential degradation pathway, as depicted in Figure 16, commencing with the following: (1) The attack of hydroxyl radicals on amines ($NH_2$), which leads to deamination [59]. (2) Subsequently, degradation of sodium atoms occurs [14], with reactive oxygen species, such as OH and $^{*}O_2$ radicals [60], represented at a wavelength of 235 nm, which vary according to the UV–Vis spectroscopy graph of dye degradations [61]. (3) The hydroxyl then separates, and nitrogen double bonds are broken by radical attacks [58], which form amine functional groups, while p-dihydroxyl biphenyl is concurrently generated [59]. (4) Hydroxyl radical attacks further lead to the formation of hydroquinone and two molecules of 3-aminonaphthalene-1-sulfonic acid [59]. (5) Following this, benzene rings begin to break down, which lead to the formation of carboxylic acids, malonic acid, acetic acid, aldehydes, alkanes, etc [62,63], and ultimately result in the mineralization of the Congo red molecule [62]. These degradation routes attest to the discoloration of Congo red to a lighter shade in water.

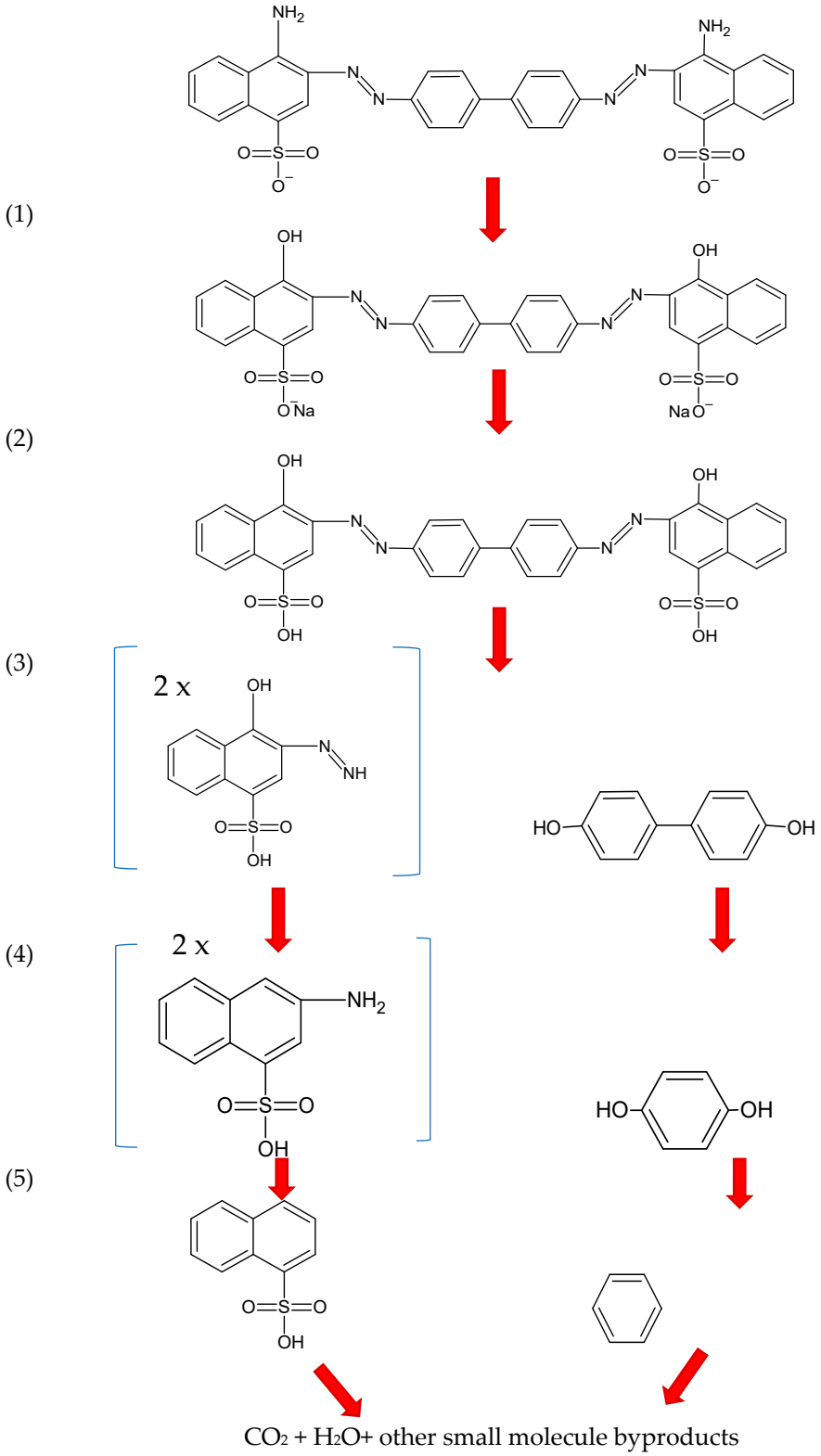


**Figure 16.** Degradation mechanism proposed for Congo red [8].

Various authors conducted similar experiments using different materials and methods. Hokonya and colleagues [15], for instance, degraded Congo red under controlled parameters and artificial light, which achieved a degradation of 15.87% in 30 min at an initial concentration of 25 ppm and 43.17% at an initial concentration of 15 ppm. They used P-$ZrO_2CeO_2ZnO$ nanoparticles in suspension as catalysts and demonstrated comparable

efficiencies in the same time frame, but with the added benefit of easy separation from the waste medium.

Hitkari and collaborators [63] also conducted controlled parameter experiments to ensure direct radiation toward the material for optimal activation. They utilized ZnO nanoparticles in suspension with copper, which achieved a degradation of 69% in 30 min using 50 mg of the synthesized sample in 50 mL of aqueous solution containing the pollutant. However, this approach led to saturation, where electromagnetic waves did not directly impact or impinge on the materials [63]. To address this, the present study employed a smaller amount of photocatalyst to enable effective degradation under normal climatic conditions.

Habibi and coworkers [64] degraded Congo red with CdS/ZnO (metal oxide chalcogenide) using a 250 W mercury lamp as a source to activate the photocatalytic material and obtained a decolorization time lapse of 105 min at a neutral pH in solution [64]. In this work, the solution was not modified because it was considered deionized water with a neutral pH. During the photocatalysis, the pH of the solution varied since the formation of the oxidizing radicals was directly related to the change in the pH of the solution.

Concerning separate materials, it was found that they have a lower efficiency, as in the work of Bessekhouad et al., who degraded an organic pollutant using $Bi_2S_3$ with $TiO_2$ methyl oxide irradiated by a solar simulator. As a result, a degradation of the pollutant was presented and it was observed that the separated materials obtained a lower efficiency (similar to the present work); however, for this work, a smaller amount of photocatalyst was used [32].

## 3. Experimental Section

The preparation of $Bi_2S_3$ thin films utilized the following reagents: bismuth nitrate (III) pentahydrate ($Bi(NO_3)_3 \cdot 5H_2O$, ≥98.0%, Sigma Aldrich Toluca, Edo. Mex., Mexico), triethanolamine (TEA)($(HOCH_2CH_2)_3N$, 99.80%, J.T. Baker, Phillipsburg, NJ, USA), sodium hydroxide (NaOH, 98.91%, CTR Scientific, Monterrey, México) and thiourea ($NH_2CSNH_2$, 99.2%, J.T. Baker).

For $TiO_2$ nanoparticles, the following reagents from Monterrey, Mexico, were used: titanium isopropoxide ($C_{12}H_{28}O_4Ti$, 97%, Sigma Aldrich), isopropanol ($C_3H_8O$, 99.8%, Fermont), and ethanol ($C_2H_5OH$, 99.5%, CTR).

ZnO nanoparticles were obtained from oxidized zinc (ZnO) extracted from the anode of a worn-out alkaline battery (type D Energizer brand).

The organic pollutant Congo red ($C_{32}H_{22}Na_2N_6O_6S_2$) from the HIMEDIA brand was employed for heterogeneous solar photocatalysis to degrade the pollutant.

### *3.1. Deposition of $Bi_2S_3$ Thin Films*

The films were deposited on glass slide substrates (soda lime glass) previously washed with acetone, isopropanol, and deionized water for 10 min in each solvent sequentially under sonication (Branson 5800, Branson Ultrasonic, Brookfield, CT, USA). For the deposition of $Bi_2S_3$ thin films, the chemical bath deposition technique was used following the methodology of Carrillo [39]. This experiment used a mixture of 5 mL of TEA (1 M) with 40 mL of $Bi(NO_3)_35H_2O$ (0.1 M), 2.5 mL of TEA ($C_6H_{15}NO_3$) (0.5 M), 2.5 mL of sodium hydroxide (NaOH) (1 M), and 5 mL of thiourea ($CH_4N_2S$) (0.15 M). After obtaining the homogeneous mixture of the precursors, 3 substrates were introduced at a temperature of 60 °C +/− 2 °C for 80 min; this process was repeated for the second and third film layers to obtain a crystalline and homogeneous film growth.

Finally, and after 80 min of chemical bath deposition, the thin films were cleaned with methanol under ultrasound for 10 min and then in deionized water in ultrasound for 10 min to finally dry the films at room temperature.

### 3.2. Preparation of $TiO_2$ Nanoparticles

For the films, the microwave-assisted sol–gel method was used for the synthesis of $TiO_2$ nanoparticles, following the methodology of Mota-González [47]. A total of 2.72 g mL of titanium isopropoxide was poured into 40 mL of isopropanol and then stirred at 700 rpm for 1 min at 80 °C; after the minute, 0.52 mL of deionized water and 1 mL of isopropanol was added and then stirred at 700 rpm for 1 min to 80 °C. The solution was then allowed to precipitate for 24 h, during which time, the two phases were separated (sol–gel), and the supernatant was removed with a pipette from the solution. To dry the solution, a microwave was used for 15 min, with intervals of 5 s of drying with 60 s of rest outside the microwave. After drying, the nanoparticles were crushed in a mortar and then washed with deionized water.

### 3.3. Preparation of the ZnO Nanoparticles

For the synthesis of ZnO nanoparticles, Energizer brand D-type discharged alkaline batteries were used following the methodology of Diaz-León et al. [65]. Wasted zinc anodes were cleaned, dried, and then leached using 10 mL of nitric acid and 20 mL of hydrogen peroxide per gram of washed powder. The resulting zinc-rich solution was used to synthesize zinc oxide nanoparticles (ZnO Nps) via sol–gel methods. For starch-based synthesis, 10 g of rice starch was dissolved in 150 mL of water, while for dextrose-based synthesis, 21.4 g of dextrose was mixed with 150 mL of water. Thermogravimetric analysis (TGA) determined the calcination temperature (400–800 °C) to convert the dried gels into ZnO NPs [65].

### 3.4. Preparation of $Bi_2S_3/TiO_2$ and $Bi_2S_3$/ZnO Thin Films

For the heterojunction of the materials, $TiO_2$ and ZnO nanoparticles were deposited on $Bi_2S_3$ films by a spin-coating technique. For the preparation of $TiO_2$ and ZnO nanoparticles, 0.02 g was dissolved in 10 mL of ethanol and then deposited at a speed of 1000 rpm for 60 s on $Bi_2S_3$ thin films. This process was repeated 4 times; afterward, the $Bi_2S_3/TiO_2$ and $Bi_2S_3$/ZnO thin films with the nanoparticles were dried at 85 °C for 15 min.

### 3.5. Characteritation of Materials

The morphology of the materials was characterized using a Hitachi SU5000 scanning electron microscope (Hitachi, Tokyo, Japan) at a voltage of 15,000 V. The elemental compositions were analyzed by EDAX quantitative analysis with a JEOL 6010 Plus (Tokyo, Japan). The crystalline structure of the materials was studied with X-ray diffraction using PANalytical (Malvern, UK) with CuKα(λ) = 1.54 Å operated at 35,000 V and 23 Ma, while scanning over 2θ in a range from 10 to 80°. Optical absorption measurements were performed using a Jeneway 6850 V/Vis spectrophotometer (Sapulpa, OK, USA) in the range of 300 nm to 1100 nm and PerkinElmer Lambda 25 UV–Vis spectrometer (Shelton, CT, USA) in a range of 300 to 750 nm, with a scan of 0.2 nm. A Kruss model DSA 30 microscope was used for the contact angle.

### 3.6. Photocatalytic Degradation of Congo Red

The photocatalytic activity of $Bi_2S_3/TiO_2$ and $Bi_2S_3$/ZnO thin films was evaluated through the degradation of the organic dye Congo red model by exposing it to solar radiation for 30 min, where three replicas were made under different climatic conditions. Table 2 shows the initial concentrations of each of the replicas and the climatic conditions when each of the replicas was performed. To prepare the aqueous solution, 80 mL of Congo red at an initial concentration of 20 ppm was prepared in a beaker while maintaining an agitation of 500 rpm [66]. At the beginning of the photocatalytic study, the thin films were introduced in such a way that they were in contact with the solution at a certain shrinkage.

After 30 min of activity, the sample was extracted with a syringe and then the concentration was evaluated in a PerkinElmer Lambda 25 UV–Vis spectrometer in a range from

300 to 750 nm. Derived from the spectrometer measurement, the percentage of degradation was evaluated (Equation (3)) [5]:

$$\%\,degradation = \frac{C_0 - C_t}{C_t} \times 100 \quad (3)$$

Additionally, the degradation time of the material was calculated from the spectrophotometer measurements using the first-order differential equation presented in Equation (4) [66]. The initial conditions were obtained to solve and calculate the maximum time required to degrade 100% of the pollutant under the same environmental conditions (Table 2) as the photocatalytic activity carried out with nanomaterials.

$$\frac{dc}{dt} = kC \quad (4)$$

## 4. Conclusions

In this study, it was established that a stable material was synthesized for use as a photocatalyst against complex organic molecules, owing to the stable structures inherent in each of the materials employed. The chemical, structural, and morphological integrity of the $Bi_2S_3$ thin film remained unaffected during the deposition of the metal oxides.

Optical characterization of the $Bi_2S_3/TiO_2$ and $Bi_2S_3/ZnO$ thin films revealed an increase in the band gap compared with the $Bi_2S_3$ thin film. Furthermore, the absorption edges exhibited a red shift upon deposition of the metal oxide nanoparticles, which indicates a broadening of the reaction spectrum relative to the $Bi_2S_3$ thin film.

Regarding the assessment of photocatalytic activity, the two-layer $Bi_2S_3/ZnO$ material demonstrated an efficiency of up to 30.80% in degrading Congo red, which is a model pollutant, within 30 min. This novel material exhibited the capability to break down molecules that contained complex organic compounds, which suggests degradation into simpler molecular forms based on UV–Vis spectroscope evaluations.

**Supplementary Materials:** The following supporting information can be downloaded from https://www.mdpi.com/article/10.3390/catal14090589/s1: Figures S1–S9: Figure S1. Transmittance of $Bi_2S_3$ thin films, Figure S2. EDX elemental analysis for thin films of two layers $Bi_2S_3/TiO_2$, Figure S3. EDX elemental analysis for thin films of three layers $Bi_2S_3/TiO_2$, Figure S4. Transmittance 2 layer $Bi_2S_3/TiO_2$ and 3 layer $Bi_2S_3/TiO_2$, Figure S5. EDX elemental analysis for thin films of two layers $Bi_2S_3/ZnO$, Figure S6. EDX elemental analysis for thin films of three layers $Bi_2S_3/ZnO$ and Figure S7. Transmittance 2 layer $Bi_2S_3/ZnO$ and 3 layer $Bi_2S_3/ZnO$, Figure S8. 2nd replica, (A) Degradation of Congo red dye, (B) Dye degradation kinetics. Figure S9. 3rd replica, (A) Degradation of Congo red dye (B) Degradation kinetics of the Congo red dye from the first replicate.

**Author Contributions:** Conceptualization, investigation, methodology, formal analysis, writing—original draft, and writing—review and editing were performed by E.P.S., C.A.R.G. and A.C.C.; investigation, writing—review and editing, visualization, and validation were performed by E.P.S., C.A.R.G., P.A.L.M., H.R.B. and A.C.C.; supervision, project administration, and funding acquisition were performed by C.A.R.G. and A.C.C. All authors have read and agreed to the published version of the manuscript.

**Funding:** This work received partial financial support from CONAHCyT through the grant CONAHCYT Postdoctoral Program 500846 and CONAHCyT through the grant SEP-CONACYT I0017-221117.

**Data Availability Statement:** The data presented in this article and Supplementary Materials are available.

**Acknowledgments:** The authors acknowledge CIMAV Unidad Mty, México, for their technical support.

**Conflicts of Interest:** The authors declare no conflicts of interest. The funders had no role in the design of the study; in the collection, analyses, or interpretation of data; in the writing of the manuscript; or in the decision to publish the results.

## References


1. Bi, S.; Jayamani, G.; Thirumalai, K.; Swaminathan, M.; Shanthi, M. Materials Today: Proceedings Solar-light assisted photocatalytic mineralization of tartrazine dye using. *Mater. Today Proc.* **2020**, *29*, 1104–1118. [CrossRef]
2. UNESCO. El valor del agua. *Ecol. Política* **2021**, *26*, 49–65.
3. Sharma, K.S.; Panchal, K.; Chhimwal, M.; Kumar, D. Integrated detection and natural remediation technology as a low-cost alternative for wastewater treatment. *Heal. Sci. Rev.* **2023**, *8*, 100111. [CrossRef]
4. Ljubas, D.; Smoljanić, G.; Juretić, H. Degradation of Methyl Orange and Congo Red dyes by using $TiO_2$ nanoparticles activated by the solar and the solar-like radiation. *J. Environ. Manage.* **2015**, *161*, 83–91. [CrossRef]
5. Ahmad, R.; Kumar, R. Adsorptive removal of congo red dye from aqueous solution using bael shell carbon. *Appl. Surf. Sci.* **2010**, *257*, 1628–1633. [CrossRef]
6. Turcu, E.; Coromelci, C.G.; Harabagiu, V.; Ignat, M. Enhancing the Photocatalytic Activity of $TiO_2$ for the Degradation of Congo Red Dye by Adjusting the Ultrasonication Regime Applied in Its Synthesis Procedure. *Catalysts* **2023**, *13*, 345. [CrossRef]
7. Moyo, S.; Makhanya, B.P.; Zwane, P.E. Use of bacterial isolates in the treatment of textile dye wastewater: A review. *Heliyon* **2022**, *8*, e09632. [CrossRef]
8. Zhu, H.; Jiang, R.; Li, J.; Fu, Y.; Jiang, S.; Yao, J. Magnetically recyclable $Fe_3O_4/Bi_2S_3$ microspheres for effective removal of Congo red dye by simultaneous adsorption and photocatalytic regeneration. *Sep. Purif. Technol.* **2017**, *179*, 184–193. [CrossRef]
9. Huang, Z.; Li, Y.; Chen, W.; Shi, J.; Zhang, N.; Wang, X.; Li, Z.; Gao, L.; Zhang, Y. Modified bentonite adsorption of organic pollutants of dye wastewater. *Mater. Chem. Phys.* **2017**, *202*, 266–276. [CrossRef]
10. Wang, X.; Deng, B.; Yu, L.; Cui, E.; Xiang, Z.; Lu, W. Degradation of azo dyes Congo red by MnBi alloy powders: Performance, kinetics and mechanism. *Mater. Chem. Phys.* **2020**, *251*, 123096. [CrossRef]
11. Kim, J.R.; Kan, E. Heterogeneous photo-Fenton oxidation of methylene blue using CdS-carbon nanotube/$TiO_2$ under visible light. *J. Ind. Eng. Chem.* **2015**, *21*, 644–652. [CrossRef]
12. Erdemoğlu, S.; Aksu, S.K.; Sayilkan, F.; Izgi, B.; Asiltürk, M.; Sayilkan, H.; Frimmel, F.; Güçer, Ş. Photocatalytic degradation of Congo Red by hydrothermally synthesized nanocrystalline $TiO_2$ and identification of degradation products by LC-MS. *J. Hazard. Mater.* **2008**, *155*, 469–476. [CrossRef]
13. Oladoye, P.O.; Ajiboye, T.O.; Omotola, E.O.; Oyewola, O.J. Methylene blue dye: Toxicity and potential elimination technology from wastewater. *Results Eng.* **2022**, *16*, 100678. [CrossRef]
14. Asses, N.; Ayed, L.; Hkiri, N.; Hamdi, M. Congo Red Decolorization and Detoxification by Aspergillus Niger: Removal Mechanisms and Dye Degradation Pathway. *Biomed Res. Int.* **2018**, *2018*. [CrossRef] [PubMed]
15. Hokonya, N.; Mahamadi, C.; Mukaratirwa-Muchanyereyi, N.; Gutu, T.; Zvinowanda, C. Green synthesis of $P-ZrO_2CeO_2ZnO$ nanoparticles using leaf extracts of Flacourtia indica and their application for the photocatalytic degradation of a model toxic dye, Congo red. *Heliyon* **2022**, *8*. [CrossRef] [PubMed]
16. Hasanpour, M.; Hatami, M. Photocatalytic performance of aerogels for organic dyes removal from wastewaters: Review study. *J. Mol. Liq.* **2020**, *309*, 113094. [CrossRef]
17. Chekir, N.; Boukendakdji, H.; Igoud, S.; Taane, W. Solar energy for the benefit of water treatment: Solar photoreactor. *Procedia Eng.* **2012**, *33*, 174–180. [CrossRef]
18. Molinari, R.; Lavorato, C.; Argurio, P. Recent progress of photocatalytic membrane reactors in water treatment and in synthesis of organic compounds. A review. *Catal. Today* **2017**, *281*, 144–164. [CrossRef]
19. Chong, M.N.; Jin, B.; Chow, C.W.K.; Saint, C. Recent developments in photocatalytic water treatment technology: A review. *Water Res.* **2010**, *44*, 2997–3027. [CrossRef]
20. Zhao, G.; Zheng, Y.; He, Z.; Lu, Z.; Wang, L.; Li, C.; Jiao, F.; Deng, C. Synthesis of $Bi_2S_3$ microsphere and its efficient photocatalytic activity under visible-light irradiation. *Trans. Nonferrous Met. Soc. China* **2018**, *28*, 2002–2010. [CrossRef]
21. Lopes, F.V.S.; Monteiro, R.A.R.; Silva, A.M.T.; Silva, G.V.; Faria, J.L.; Mendes, A.M.; Vilar, V.J.P.; Boaventura, R.A.R. Insights into UV-$TiO_2$ photocatalytic degradation of PCE for air decontamination systems. *Chem. Eng. J.* **2012**, *204–206*, 244–257. [CrossRef]
22. Byrne, C.; Subramanian, G.; Pillai, S.C. Recent advances in photocatalysis for environmental applications. *J. Environ. Chem. Eng.* **2018**, *6*, 3531–3555. [CrossRef]
23. Jayanthi Kalaivani, G.; Suja, S.K. $TiO_2$(rutile) embedded inulin—A versatile bio-nanocomposite for photocatalytic degradation of methylene blue. *Carbohydr. Polym.* **2016**, *143*, 51–60. [CrossRef] [PubMed]
24. Xiaofang, C.; Jia, Z.; Yuning, H.U.O.; Hexing, L.I. Preparation and visible light catalytic activity of three—Dimensional ordered macroporous CdS/$TiO_2$ films. *Chin. J. Catal.* **2013**, *34*, 949–955. [CrossRef]
25. Wu, T.; Zhou, X.; Zhang, H.; Zhong, X. Bi2S3 Nanostructures: A New Photocatalyst. *Nano Res.* **2010**, *3*, 379–386. [CrossRef]
26. Liu, B.; Wen, L.; Zhao, X. Progress in Organic Coatings Efficient degradation of aqueous methyl orange over TiO2 and CdS electrodes using photoelectrocatalysis under UV and visible light irradiation. *Prog. Org. Coat.* **2009**, *64*, 120–123. [CrossRef]
27. Lv, T.; Pan, L.; Liu, X.; Sun, Z. Electrochimica Acta Visible-light photocatalytic degradation of methyl orange by CdS—$TiO_2$—Au composites synthesized via microwave-assisted reaction. *Electrochim. Acta* **2012**, *83*, 216–220. [CrossRef]
28. Yan, X.; Yuan, K.; Lu, N.; Xu, H.; Zhang, S.; Takeuchi, N.; Kobayashi, H.; Li, R. The interplay of sulfur doping and surface hydroxyl in band gap engineering: Mesoporous sulfur-doped $TiO_2$coupled with magnetite as a recyclable, efficient, visible light active photocatalyst for water purification. *Appl. Catal. B Environ.* **2017**, *218*, 20–31. [CrossRef]

29. Peng, S.; Huang, Y.; Li, Y. Rare earth doped TiO2-CdS and TiO2-CdS composites with improvement of photocatalytic hydrogen evolution under visible light irradiation. *Mater. Sci. Semicond. Process.* **2013**, *16*, 62–69. [CrossRef]
30. Cebriano, T.; García-Díaz, I.; Fernández, A.L.; Fernández, P.; López, F.A. Synthesis and characterization of ZnO micro- and nanostructures grown from recovered ZnO from spent alkaline batteries. *J. Environ. Chem. Eng.* **2017**, *5*, 2903–2911. [CrossRef]
31. Balachandran, S.; Swaminathan, M. The simple, template free synthesis of a $Bi_2S_3$-ZnO heterostructure and its superior photocatalytic activity under UV-A light. *Dalt. Trans.* **2013**, *42*, 5338–5347. [CrossRef] [PubMed]
32. Bessekhouad, Y.; Robert, D.; Weber, J.V. $Bi_2S_3/TiO_2$ and $CdS/TiO_2$ heterojunctions as an available configuration for photocatalytic degradation of organic pollutant. *J. Photochem. Photobiol. A Chem.* **2004**, *163*, 569–580. [CrossRef]
33. Liu, W.; He, T.; Wang, Y.; Ning, G.; Xu, Z.; Chen, X. Synergistic adsorption—Photocatalytic degradation effect and norfloxacin mechanism of ZnO/ZnS @ BC under UV—light irradiation. *Sci. Rep.* **2020**, *10*, 11903. [CrossRef]
34. Schneider, J.; Matsuoka, M.; Takeuchi, M.; Zhang, J.; Horiuchi, Y.; Anpo, M.; Bahnemann, D.W. Understanding TiO2photocatalysis: Mechanisms and materials. *Chem. Rev.* **2014**, *114*, 9919–9986. [CrossRef]
35. Biswas, K.; Zhao, L.D.; Kanatzidis, M.G. Tellurium-free thermoelectric: The anisotropic n-type semiconductor $Bi_2S_3$. *Adv. Energy Mater.* **2012**, *2*, 634–638. [CrossRef]
36. Salunkhe, D.B.; Dubal, D.P.; Sali, J.V.; Sankapal, B.R. Linker free synthesis of $TiO_2/Bi_2S_3$ heterostructure towards solar cell application: Facile chemical routes. *Mater. Sci. Semicond. Process.* **2015**, *30*, 335–342. [CrossRef]
37. Yang, L.; Sun, W.; Luo, S.; Luo, Y. White fungus-like mesoporous Bi2S3 ball/TiO2 heterojunction with high photocatalytic efficiency in purifying 2,4-dichlorophenoxyacetic acid/Cr(VI) contaminated water. *Appl. Catal. B Environ.* **2014**, *156–157*, 25–34. [CrossRef]
38. Spasiano, D.; Marotta, R.; Malato, S.; Fernandez-Iba??ez, P.; Di Somma, I. Solar photocatalysis: Materials, reactors, some commercial, and pre-industrialized applications. A comprehensive approach. *Appl. Catal. B Environ.* **2015**, *170–171*, 90–123. [CrossRef]
39. Carrillo-castillo, A.; Rivas-valles, B.G.; Castillo, S.J.; Ramirez, M.M.; Luque-morales, P.A. SS symmetry New Formulation to Synthetize Semiconductor $Bi_2S_3$ Thin Films Using Chemical Bath Deposition for Optoelectronic Applications. *Symmetry* **2022**, *14*, 2487. [CrossRef]
40. Demir, H.; Şahin, Ö.; Baytar, O.; Horoz, S. Investigation of the properties of photocatalytically active Cu-doped—$Bi_2S_3$ nanocomposite catalysts. *J. Mater. Sci. Mater. Electron.* **2020**, *2*, 10347–10354. [CrossRef]
41. Lokhande, R.S.; Thakur, S.R.; Chate, P.A. Chemical deposition of bismuth sulphide thin films using malonic acid ligand. *Optik* **2020**, *219*, 165230. [CrossRef]
42. Shinde, N.S.; Rath, M.C.; Dhaigude, H.D.; Lokhande, C.D.; Fulari, V.J. Characterization of electrodeposited Bi2S3 thin films by holographic interferometry. *Opt. Commun.* **2009**, *282*, 3127–3131. [CrossRef]
43. Momeni, M.; Saghafian, H.; Golestani-Fard, F.; Barati, N.; Khanahmadi, A. Effect of $SiO_2$ addition on photocatalytic activity, water contact angle and mechanical stability of visible light activated $TiO_2$ thin films applied on stainless steel by a sol gel method. *Appl. Surf. Sci.* **2017**, *392*, 80–87. [CrossRef]
44. Rong, Y.; Yang, Z.; Deng, L.; Fu, Z. ZnO@Ag microspheres used as the anodic materials of superior alkaline rechargeable Zn–Ni batteries. *Ceram. Int.* **2020**, *46*, 16908–16917. [CrossRef]
45. Shah, A.H.; Rather, M.A. Effect of calcination temperature on the crystallite size, particle size and zeta potential of $TiO_2$ nanoparticles synthesized via polyol-mediated method. *Mater. Today Proc.* **2021**, *44*, 482–488. [CrossRef]
46. Wu, Z.; Yuan, D.; Lin, S.; Guo, W.; Zhan, D.; Sun, L.; Lin, C. Enhanced photoelectrocatalytic activity of $Bi_2S_3$–$TiO_2$ nanotube arrays hetero-structure under visible light irradiation. *Int. J. Hydrogen Energy* **2020**, *45*, 32012–32021. [CrossRef]
47. Mota-gonzález, M.; Hernández-carrillo, H.; Alaniz-hernandez, M. $TiO_2$ obtenido por el proceso sol gel asistido con microondas. *Lat. Am. J. Appl. Eng.* **2018**, *3*, 12–15. [CrossRef]
48. Kumar, S.; Sharma, S.; Sood, S.; Umar, A.; Kansal, S.K. Bismuth sulfide ($Bi_2S_3$) nanotubes decorated TiO2 nanoparticles heterojunction assembly for enhanced solar light driven photocatalytic activity. *Ceram. Int.* **2016**, *42*, 17551–17557. [CrossRef]
49. Sarentuya; Bai, H. Amurishana Synthesis of $Bi_2S_3$-$TiO_2$ nanocomposite and its electrochemical and enhanced photocatalytic properties for phenol degradation. *Int. J. Electrochem. Sci.* **2023**, *18*, 100071. [CrossRef]
50. Carvalho, H.W.P.; Batista, A.P.L.; Hammer, P.; Ramalho, T.C. Photocatalytic degradation of methylene blue by TiO2-Cu thin films: Theoretical and experimental study. *J. Hazard. Mater.* **2010**, *184*, 273–280. [CrossRef]
51. Bagheri, M.; Mahjoub, A.R.; Mehri, B. Enhanced photocatalytic degradation of congo red by solvothermally synthesized CuInSe2-ZnO nanocomposites. *RSC Adv.* **2014**, *4*, 21757–21764. [CrossRef]
52. AL-Zahrani, A.A.; Zainal, Z.; Talib, Z.A.; Lim, H.N.; Holi, A.M. Bismuth sulphide decorated ZnO nanorods heterostructure assembly via controlled SILAR cationic concentration for enhanced photoelectrochemical cells. *Mater. Res. Express* **2020**, *7*, 025510. [CrossRef]
53. Qi, K.; Cheng, B.; Yu, J.; Ho, W. Review on the improvement of the photocatalytic and antibacterial activities of ZnO. *J. Alloys Compd.* **2017**, *727*, 792–820. [CrossRef]
54. Nikam, P.R.; Baviskar, P.K.; Sali, J.V.; Gurav, K.V.; Kim, J.H.; Sankapal, B.R. SILAR coated $Bi_2S_3$ nanoparticles on vertically aligned ZnO nanorods: Synthesis and characterizations. *Ceram. Int.* **2015**, *41*, 10394–10399. [CrossRef]
55. Yu, H.; Wu, Z.; Dong, Y.; Huang, C.; Shi, S.; Zhang, Y. ZnO nanorod arrays modified with Bi2S3 nanoparticles as cathode for efficient polymer solar cells. *Org. Electron.* **2019**, *75*, 105369. [CrossRef]

56. Ye, F.; Qian, J.; Xia, J.; Li, L.; Wang, S.; Zeng, Z.; Mao, J.; Ahamad, M.; Xiao, Z.; Zhang, Q. Efficient photoelectrocatalytic degradation of pollutants over hydrophobic carbon felt loaded with Fe-doped porous carbon nitride via direct activation of molecular oxygen. *Environ. Res.* **2024**, *249*, 118497. [CrossRef] [PubMed]
57. Wang, S.; Luo, C.; Tan, F.; Cheng, X.; Ma, Q.; Wu, D.; Li, P.; Zhang, F.; Ma, J. Degradation of Congo red by UV photolysis of nitrate: Kinetics and degradation mechanism. *Sep. Purif. Technol.* **2021**, *262*, 118276. [CrossRef]
58. Argote-Fuentes, S.; Feria-Reyes, R.; Ramos-Ramírez, E.; Gutiérrez-Ortega, N.; Cruz-Jiménez, G. Photoelectrocatalytic degradation of congo red dye with activated hydrotalcites and copper anode. *Catalysts* **2021**, *11*, 211. [CrossRef]
59. Telke, A.A.; Joshi, S.M.; Jadhav, S.U.; Tamboli, D.P.; Govindwar, S.P. Decolorization and detoxification of Congo red and textile industry effluent by an isolated bacterium *Pseudomonas* sp. SU-EBT. *Biodegradation* **2010**, *21*, 283–296. [CrossRef]
60. Thomas, M.; Naikoo, G.A.; Sheikh, M.U.D.; Bano, M.; Khan, F. Effective photocatalytic degradation of Congo red dye using alginate/carboxymethyl cellulose/$TiO_2$ nanocomposite hydrogel under direct sunlight irradiation. *J. Photochem. Photobiol. A Chem.* **2016**, *327*, 33–43. [CrossRef]
61. Asaad Mahdi, M.; Farhan, M.A.; Mahmoud, Z.H.; Mahdi Rheima, A.; sabri Abbas, Z.; Kadhim, M.M.; Dhari Jawad Al-Bayati, A.; Salam Jaber, A.; Hachim, S.K.; Hussain Ismail, A. Direct sunlight photodegradation of congo red in aqueous solution by $TiO_2$/rGO binary system: Experimental and DFT study. *Arab. J. Chem.* **2023**, *16*, 104992. [CrossRef]
62. Muneer, M.; Saeed, M.; Bhatti, I.A.; Haq, A.U.; Khosa, M.K.; Jamal, M.A.; Ali, S. Radiation induced degradation of Congo red dye: A mechanistic study. *Nukleonika* **2019**, *64*, 49–53. [CrossRef]
63. Hitkari, G.; Chowdhary, P.; Kumar, V.; Singh, S.; Motghare, A. Potential of Copper-Zinc Oxide nanocomposite for photocatalytic degradation of congo red dye. *Clean. Chem. Eng.* **2022**, *1*, 100003. [CrossRef]
64. Habibi, M.H.; Rahmati, M.H. The effect of operational parameters on the photocatalytic degradation of Congo red organic dye using ZnO-CdS core-shell nano-structure coated on glass by Doctor Blade method. *Spectrochim. Acta Part A Mol. Biomol. Spectrosc.* **2015**, *137*, 160–164. [CrossRef]
65. Díaz De León, C.L.; Olivas-Armendariz, I.; Hernández Paz, J.F.; Gómez-Esparza, C.D.; Reyes-Blas, H.; Hernández González, M.; Velasco-Santos, C.; Rivera-Armenta, J.L.; Rodríguez-González, C.A. Synthesis by sol-gel and cytotoxicity of Zinc Oxide nanoparticles using wasted alkaline batteries. *Dig. J. Nanomater. Biostructures* **2017**, *12*, 371–379.
66. Palma-Soto, E.; MOTA-GONZÁLEZ, M.; Luque-Morales, P.A.; Carrillo-Castillo, A. Determination of photocatalytic activity for the system: CdS chemical bath deposited thin films coated with $TiO_2$ NPs. *Chalcogenide Lett.* **2021**, *18*, 47–58. [CrossRef]